



Enhanced photocatalytic activity of ternary Ag/g-C₃N₄/NaTaO₃ photocatalysts under wide spectrum light radiation: The high potential band protection mechanism

Lin Tang^{a,b,*}, Chengyang Feng^{a,b}, Yaocheng Deng^{a,b}, Guangming Zeng^{a,b,*}, Jiajia Wang^{a,b},
Yani Liu^{a,b}, Haopeng Feng^{a,b}, Jingjing Wang^{a,b}

^a College of Environmental Science and Engineering, Hunan University, Changsha, 410082, China

^b Key Laboratory of Environmental Biology and Pollution Control, Hunan University, Ministry of Education, Changsha, 410082, China

ARTICLE INFO

Keywords:

Photocatalysis
NaTaO₃
g-C₃N₄
Z-scheme mechanism
Wide-spectrum light response

ABSTRACT

Constructing heterojunction photocatalyst is an effective method to enhance the separation of photogenerated electron and hole and benefit the wide-bandgap photocatalyst with significant visible light response ability. In this study, a novel and highly efficient ternary photocatalyst was prepared by depositing Ag nanoparticles on the surface of graphitic carbon nitride nanosheets (g-C₃N₄)/NaTaO₃ nanohybrid. It showed an enhanced photocatalytic degradation of tetracycline (TC), rhodamine B (RhB) and phenol under wide-spectrum light irradiation. Compared to pure NaTaO₃, g-C₃N₄ and binary g-C₃N₄/NaTaO₃, Ag/g-C₃N₄/NaTaO₃ displayed enhanced photodegradation efficiency with 95.47% removal of TC (20 mg/L) in 60 min under visible light irradiation. From the free radical quenching experiment and ESR characterization results, the charge transfer process can be identified as a Z-scheme transfer mechanism, which can significantly enhance the charge separation rate and protect the high potential valence band (VB) of NaTaO₃ and conduction band (CB) of g-C₃N₄. This work provides a new promising approach for designing novel Z-scheme photocatalysts.

1. Introduction

In recent years, photocatalytic technology has been considered as the most promising technology to solve water pollution problems. However, most of the semiconductor photocatalysts are only photo-excited by ultraviolet (UV) light which only accounts for 4% of the whole sunlight spectrum. Therefore, it is imperative to develop more wide-spectrum light driven photocatalysts. Graphite carbon nitride (g-C₃N₄), a novel type of metal-free narrow bandgap semiconductor catalyst, shows excellent photocatalytic activity for organic pollutants degradation under visible light irradiation [1,2]. But the photocatalytic activities of g-C₃N₄ are limited because of its serious recombination of photogenerated electron-hole pairs and small specific surface area.

Large numbers of methods have been developed to enlarge the light absorption range and accelerate charge separation rate of semiconductor photocatalysts [3–6], among which, fabricating heterojunction photocatalyst is an effective way to obtain significant visible light response. For example, Li et al. [7] developed DyVO₄/g-C₃N₄I composite photocatalysts to degrade dyes under visible light irradiation, and Yan et al. [8] prepared N-doped ZnO/g-C₃N₄ core-shell photocatalysts

with high visible-light activity for the degradation of Rhodamin B. The photogenerated electrons and holes on heterojunction can transfer and accumulate on different compositions, which greatly improves the charge separation rate and light utilization.

Tantalates have appropriate semiconducting nature and highly positive valence band (VB). The VB potential of NaTaO₃ (+3.87 eV) is much higher than many other semiconductors such as TiO₂ (+2.91 eV), which gives the photogenerated holes higher oxidative activity, and the conduction band (CB) of tantalates is more negative compared to titanates due to its Ta5d orbital. However, suffering from low response of visible light and serious recombination of photogenerated electron-hole pairs, pure tantalates have very poor performance in degradation of pollutants. Xu et al. [9] prepared Ag/AgCl/NaTaO₃ nanocubes with high visible-light response. As light sensitive materials, Ag/AgCl on the surface of NaTaO₃ can enhance the photocatalytic activities under visible light irradiation. However, due to its band structure, most of the electrons and holes generated on the heterojunction will shift to AgCl, which lead to its limited ability to improve charge separation. Fortunately, the suitable energy band structure of NaTaO₃ and g-C₃N₄ raises the possibility of fabricating g-C₃N₄/NaTaO₃ heterojunction.

* Corresponding authors at: College of Environmental Science and Engineering, Hunan University, Changsha, 410082, China.
E-mail addresses: tanglin@hnu.edu.cn (L. Tang), zgming@hnu.edu.cn (G. Zeng).

Electrons and holes can accumulate on the CB of NaTaO₃ and the VB of g-C₃N₄, respectively, which is more favorable to charge separation.

However, the reactivity of photogenerated electrons and holes were depressed through the transfer in general heterojunction structure [10–12], where the photogenerated electrons will accumulate on a more negative CB of a semiconductor component, and the photogenerated holes will transfer to a more positive VB of the coupled semiconductor. Z-scheme heterojunction photocatalysts are exactly what we need, which have excellent light absorptivity and high charge separation rate, and the most important is that they can provide protection for highly reactive photogenerated electrons and holes. In Z-scheme heterojunction, photogenerated charges can accumulate on the higher potential energy band rather than transfer to the lower energy band, so that the high potential energy band can be protected, and the electrons and holes can maintain high reactivity. Up to now, many Z-scheme photocatalysts have been developed, such as CdS/Au/TiO₂ and BiVO₄/Ag/Cu₂O [13,14]. In these works, the introduction of precious metals changed the carrier transfer process into Z-scheme mechanism, through which the photogenerated carriers of the VB of TiO₂ and BiVO₄ and the CB of CdS and Cu₂O can be made full use of, and the protection of high potential energy band ensures higher reaction activity of photogenerated carriers.

Herein, we improved preparation method to obtain g-C₃N₄ nanosheet with higher specific surface area and fabricated g-C₃N₄/NaTaO₃ heterojunction to inhibit the recombination of photogenerated electron-hole pairs. Furthermore, Ag nanoparticles were deposited on the surface of g-C₃N₄/NaTaO₃ nanohybrid via a photoreduction method. The Ag nanoparticle can improve visible light response by surface plasmon resonance (SPR), acting as a charge bridge between g-C₃N₄ and NaTaO₃ and changing the carrier transfer process into a Z-scheme transfer mechanism. The Z-scheme mechanism can successfully protect the high potential VB of NaTaO₃ and CB of g-C₃N₄. The enhanced photocatalytic activity of Ag/g-C₃N₄/NaTaO₃ photocatalysts was tested by degrading TC, RhB and phenol under UV light, visible light and near-infrared light irradiation.

2. Experimental section

2.1. Chemicals

Tantalum oxide (Ta₂O₅), sodium hydroxide (NaOH), silver nitrate (AgNO₃), melamine (C₃N₃(NH₂)₃), ethylene glycol ((CH₂OH)₂), methanol (CH₃OH), ethanol (CH₃CH₂OH), tetracycline (TC), rhodamine B (RhB) and phenol were purchased from Sinopharm Chemical Regent Co. Ltd (Shanghai, China). All of the reagents were analytical grade and used without further purification. Deionized water was used in the whole experiment.

2.2. Preparation of NaTaO₃ nanocube

NaTaO₃ nanocubes were synthesized by the reported hydrothermal method. In a typical procedure, 1.20 g NaOH was added into 30 mL deionized water, and 0.442 g Ta₂O₅ was added into 10 mL ethylene glycol. The two solutions were mixed in a beaker and finally added into a Teflon-lined stainless steel autoclave (50 mL capacity) after magnetic stirring for 2 h. The autoclave was kept at a temperature of 140 °C for 12 h. After cooling to room temperature, the resulting precipitates were collected by filtration, washed with deionized water and ethanol several times and dried at 80 °C for 12 h.

2.3. Preparation of g-C₃N₄ nanosheet

The g-C₃N₄ nanosheet was prepared by a modified method based on the previous publication [15]. Typically, melamine was put into a covered ceramic crucible and heated to 500 °C at a rate of 2 °C/min and maintained at 500 °C for 3 h. After cooling to ambient temperature, the

yellow agglomerates were obtained and grounded into powder. Then, the obtained yellow powder was put into a ceramic crucible covered with silver paper and heated at 550 °C at a heating rate of 2 °C/min and kept at 550 °C for 2 h. Finally the yellowish-white powdered g-C₃N₄ was obtained.

2.4. Preparation of g-C₃N₄/NaTaO₃ heterojunction

The g-C₃N₄/NaTaO₃ heterojunction photocatalyst was prepared by a wet-impregnation and facile calcination method. At first, the different amount of g-C₃N₄ was dispersed in beakers with same volume of methanol, separately. Then, the as-prepared NaTaO₃ was added and sonicated for 2 h. The mixtures were kept stirring in a fume cupboard until volatilization of the methanol, and the obtained product was dried at 60 °C and ground into powder. Then the powder was transferred into a covered ceramic crucible and heated at 500 °C at a heating rate of 2 °C/min for 3 h. After cooling to ambient temperature, the g-C₃N₄/NaTaO₃ heterojunction photocatalyst was obtained.

2.5. Preparation of Ag/g-C₃N₄/NaTaO₃ ternary photocatalyst

The Ag/g-C₃N₄/NaTaO₃ ternary photocatalyst was prepared by a facile photo-deposition process. Typically, 1.0 g of g-C₃N₄/NaTaO₃ nanocomposite and certain amount of AgNO₃ solution (20 mg/mL) were added into 50 mL methanol solution (containing 10 mL methanol). The mixture solution was stirred under the irradiation of a 300 W Xe lamp for 1 h. The final product was collected by filtration and washed with deionized water and ethanol for several times and dried at 60 °C for 12 h.

2.6. Characterization

The crystal structures of the prepared samples were characterized by X-ray diffractometer (Bruker AXS D8 Advances) with the Cu-K α irradiation source at a scanning rate (2 θ) of 4° min⁻¹ from 10° to 80°. The morphologies were measured by a Hitachi S-4800 field emission scanning electron microscopy (FE-SEM, Hitachi, Japan) and a F20 S-TWIN transmission electron microscopy (TEM, Tecnai G2, FEI Co). Fourier transform infrared spectroscopy (FTIR) was measured on an IR Prestige-21 spectrometer using the standard KBr disk method. The X-ray photoelectron spectroscopy (XPS) was employed by a Thermo ESCALAB 250XI spectrometer with Al K α source. The UV–vis diffused reflectance spectra (UV–vis DRS) were obtained by a UV–vis spectrophotometer (Cary 300, USA) with an integrating sphere attachment, using BaSO₄ as the reference. The photoluminescence (PL) spectroscopy was obtained by a Hitachi-7000 fluorescence spectrometer. The total organic carbon (TOC) assays were measured by a Shimadzu TOC-VCPH analyzer. The N₂ sorption isotherms were obtained by a Nova 2200e analytical system at 77 K. The specific surface area was calculated by Brunauer–Emmett–Teller (BET) method. The electron spin resonance (ESR) signals of free radicals was examined by using 5,5-dimethyl-1-pyrroline N-oxide (DMPO) as a probe on a Bruker ER200-SRC spectrometer under visible light irradiation (λ > 420 nm).

2.7. Photoelectrochemical measurements

The photoelectrochemical responses of the prepared catalysts were measured by a three-electrode cell and a CHI 660D workstation. A Pt electrode and an Ag/AgCl electrode were employed as the counter electrode and reference electrode respectively. FTO electrodes covered in photocatalysts were used as the working electrode. 0.2 M Na₂SO₄ solution was used as supporting electrolyte in this system [16]. A 300 W Xe lamp with different wavelength cut-off filters was used as light source.

2.8. Photocatalytic activity test

The photocatalytic activity of the as-prepared photocatalysts was investigated by the degradation of TC under UV, visible and near infrared light irradiation. A 300 W Xe lamp with different wavelength cut-off filters was used as light source. In a typical procedure, 50 mg as-prepared catalyst was mixed with 50 mL TC solution (20 mg/L) and stirred for 30 min in the dark. After achieving the adsorption-desorption equilibrium, the reaction system was exposed to the 300 W Xe lamp with continues stir. The reaction solution was collected and analyzed by UV-vis spectrophotometer every 10 min. Moreover, RhB (20 mg/L) and phenol (20 mg/L) were also used as additional processing object to test the applicability of the as-prepared catalysts. And the used catalyst was collected by filtration and used for another run to test the stability of the catalyst. The existence of active species was detected by trapping experiments. Ethylenediaminetetraacetic acid disodium (EDTA-2Na), 2-propanol (IPA) and 1,4-benzoquinone (BQ) were used as the hole (h^+) scavenger, hydroxyl radical ($\cdot OH$) scavenger and superoxide radical ($\cdot O_2^-$) scavenger, respectively. And $\cdot OH$ and $\cdot O_2^-$ radicals were also tested by the ESR techniques.

3. Result and discussion

3.1. Characterization of as-prepared catalysts

The typical X-ray diffraction (XRD) pattern of the obtained pure $NaTaO_3$ nanocubes, pure $g-C_3N_4$ nanosheets, $g-C_3N_4/NaTaO_3$ heterojunctions and $Ag/g-C_3N_4/NaTaO_3$ photocatalysts are displayed in Fig. 1A. The diffraction pattern for pure $NaTaO_3$ nanocubes exhibits seven distinct peaks at 22.9° , 32.5° , 40.1° , 46.6° , 52.5° , 58.0° and 68.0° , which correspond to (020), (200), (220), (202), (301), (321) and (400) crystal planes of $NaTaO_3$ (JCPDS card No. 25-0863), respectively [17,18], and the obtained $NaTaO_3$ powders can be classified as orthorhombic structure according to the JCPDS card (25-0863). The diffraction peaks of $NaTaO_3$ are obvious and intense which indicates the highly crystalline nature of $NaTaO_3$ nanocubes. And two diffraction peaks of $g-C_3N_4$ can be found at 12.7° and 27.8° , which correspond to the (100) and (002) crystal planes (JCPDS 50-1250), respectively [19,20]. The peak (100) corresponds to the interplanar packing of heptazine units [21], and the peak (002) is a typical feature of inter-layer stacking structure of conjugated aromatic system, which suggests the graphite-like structure of $g-C_3N_4$ [22,23]. The diffraction peaks of binary $g-C_3N_4/NaTaO_3$ sample and ternary $Ag/g-C_3N_4/NaTaO_3$ sample

are exactly similar to the peak of pure $NaTaO_3$, which indicates that the crystal structure of $NaTaO_3$ nanocubes was not destroyed by the combination with $g-C_3N_4$ nanosheets and Ag nanoparticles. A weak peak can be observed in the diffraction pattern of $g-C_3N_4/NaTaO_3$ and $Ag/g-C_3N_4/NaTaO_3$ near 27.8° , which demonstrates the successful combination of $g-C_3N_4$ and $NaTaO_3$. The peak of Ag cannot be found in the diffraction pattern of $Ag/g-C_3N_4/NaTaO_3$, which is presumably because only a small amount of Ag nanoparticles were deposited on the surface of photocatalysts. Furthermore, no impurity peaks are observed in all patterns, confirming high purity of the obtained catalysts.

Typical morphologies and nanostructure of prepared samples were investigated by SEM and TEM as shown in Fig. 1B–H. It can be seen from Fig. 1B and C that pure $NaTaO_3$ presents a typical nanocube structure with highly smooth surface. The SEM imaging of binary $g-C_3N_4/NaTaO_3$ is shown in Fig. 1D, from which, a layer of floccules adhering on the surface of $NaTaO_3$ nanocubes can be observed, and these floccules are identified as $g-C_3N_4$. Compared with pure $NaTaO_3$, the binary $g-C_3N_4/NaTaO_3$ samples have much rougher surface. The TEM images of $g-C_3N_4/NaTaO_3$ (Fig. 1E and F) more clearly show that the photocatalysts are composed of $NaTaO_3$ nanocubes and $g-C_3N_4$ nanosheets. As demonstrate in Fig. 1G and H, the Ag nanoparticles were obviously deposited on the surface of $NaTaO_3$ nanocubes and $g-C_3N_4$ nanosheets. Some of the Ag nanoparticles were distributed on the contact interface between $NaTaO_3$ and $g-C_3N_4$, which can act as electronic bridge and facilitate the charge transfer between $NaTaO_3$ and $g-C_3N_4$. Fig. S1A and B display the TEM images of $Ag/g-C_3N_4/NaTaO_3$ before and after being bombarded by high intensity electron beam. It is clear that all the nanoparticles disappeared after the electron-beam bombardment, which can be attributed to the melting of Ag nanoparticles under the bombardment. The EDS analysis (Fig. S1C) further revealed that the silver elements were contained in the $Ag/g-C_3N_4/NaTaO_3$ samples. The above results indicate the formation of ternary $Ag/g-C_3N_4/NaTaO_3$ photocatalysts, and this ternary structure might play a decisive role in enhancing photocatalytic performance.

The chemical composition and structure of the prepared catalysts were preliminary analyzed by FTIR spectra. As shown in Fig. S2, the peaks located at 1241 , 1319 , 1410 , 1570 and 1640 cm^{-1} (marked with “*”) belonged to the typical stretching vibration modes of the $g-C_3N_4$ heterocycles [24]. The peak located at 451 cm^{-1} (marked with “#”) was identified as the characteristic peak of $NaTaO_3$. All the characteristic peaks of $g-C_3N_4$ and $NaTaO_3$ could be observed obviously in both binary and ternary complex catalyst, which suggested that the complex catalysts were successfully synthesized. Due to the small amount of

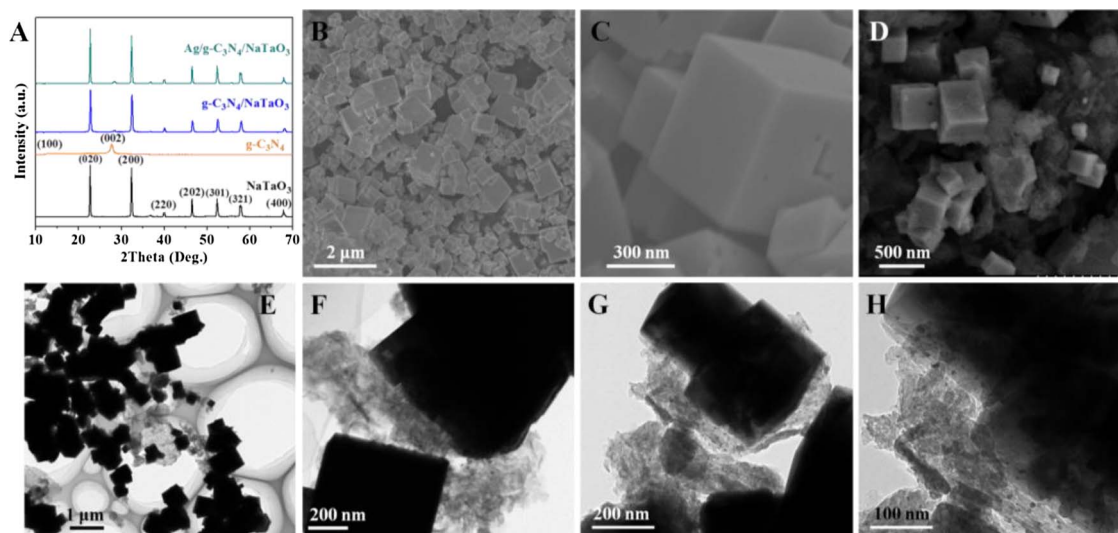


Fig. 1. XRD pattern of as-prepared samples (A); SEM images of (B, C) pure $NaTaO_3$ nanocubes, (D) $g-C_3N_4/NaTaO_3$; TEM images of (E, F) $g-C_3N_4/NaTaO_3$ and (G, H) $Ag/g-C_3N_4/NaTaO_3$.

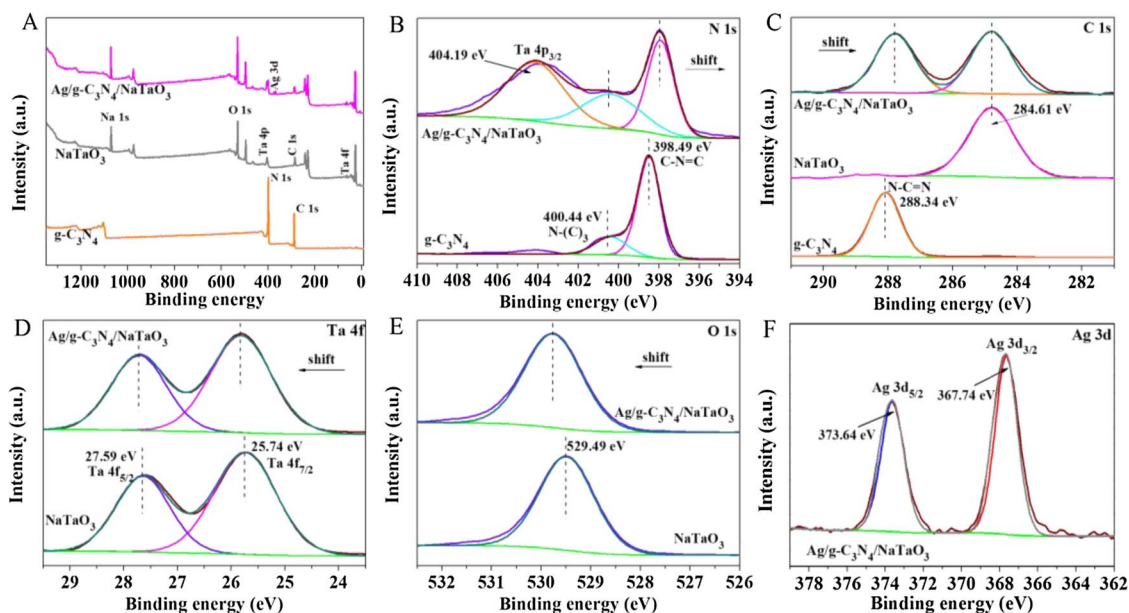


Fig. 2. XPS spectra of pure $g\text{-C}_3\text{N}_4$, NaTaO_3 and $\text{Ag/g-C}_3\text{N}_4/\text{NaTaO}_3$ nanocomposite: (A) survey, (B) N 1s, (C) C 1s, (D) Ta 4f, (E) O 1s and (F) Ag 3d.

metallic Ag, no discernable emerging peaks could be observed in ternary catalyst, which also indicated that the introduction of Ag did not change the structure of $g\text{-C}_3\text{N}_4$ and NaTaO_3 .

XPS was also used to further characterize the elemental chemical compositions and chemical status of the obtained photocatalysts. As shown in the survey XPS spectrum of $\text{Ag/g-C}_3\text{N}_4/\text{NaTaO}_3$ (Fig. 2A), several major peaks can be observed, indicating that the main elements of the prepared photocatalysts are C, N, Na, Ta, O and Ag. Fig. 2B shows the N 1s spectrum in $g\text{-C}_3\text{N}_4$ and $\text{Ag/g-C}_3\text{N}_4/\text{NaTaO}_3$. The N 1s spectrum can be divided into two peaks at 398.49 eV and 400.44 eV, clearly evidencing the presence of two chemical environments for nitrogen atoms. The peak at 398.49 eV belongs to sp^2 -hybridized nitrogen in $\text{C}=\text{N}=\text{C}$, and the peak at 400.44 eV belongs to the tertiary nitrogen ($\text{N}-(\text{C})_3$) groups [15]. After the composition with NaTaO_3 , an obvious peak located at 404.19 eV belonging to Ta $4p_{3/2}$ can be observed nearby the N 1s peaks, and the peak signals of N 1s shift to lower binding energy. In Fig. 2C, the C 1s peak of $g\text{-C}_3\text{N}_4$ located at 288.34 eV can be attributed to the $\text{C}=\text{C}-\text{C}$ bond [22]. The peak signals of C 1s also shift to lower binding energy after combining with NaTaO_3 , and it should be noticed that the binding energy of standard carbon peak (284.61 eV) is not changed before and after combination. The Ta spectrum in Fig. 2D displays two peaks located at 27.59 eV and 25.74 eV, which can be attributed to Ta $4f_{5/2}$ and Ta $4f_{7/2}$ from NaTaO_3 [17]. The peak at 529.49 eV can be assigned to O 1s (Fig. 2E). Both the binding energy of Ta 4f and O 1s are slightly shifted to a higher position after combining NaTaO_3 with $g\text{-C}_3\text{N}_4$. As the change of binding energy in XPS spectra can be attributed to the intense interaction between each composition, the existence of heterostructure interaction in as-prepared $\text{Ag/g-C}_3\text{N}_4/\text{NaTaO}_3$ can be implied by the XPS measurements. Fig. 2F shows the high-resolution XPS spectra of Ag 3d, where two main peaks located at 373.64 eV and 367.74 eV can be assigned to the metallic Ag from photo-reduction process [25]. The results confirm that metallic Ag was obtained on the surface of as-prepared photocatalysts.

3.2. Photoelectric properties of obtained photocatalysts

UV/vis diffuse reflectance spectrum (DRS) was measured to evaluate the light absorption of pure NaTaO_3 , $g\text{-C}_3\text{N}_4$ and binary $g\text{-C}_3\text{N}_4/\text{NaTaO}_3$ heterojunction and ternary $\text{Ag/g-C}_3\text{N}_4/\text{NaTaO}_3$ catalyst, and the test results were compared in Fig. 3A. It is obvious that the pure NaTaO_3 sample shows excellent absorbency in UV light region.

However, almost no absorbance in visible light region can be found due to its wide bandgap. The $g\text{-C}_3\text{N}_4$ is able to absorb the visible-light irradiation as its optical absorption edge was estimated to be about 450 nm. After coupling $g\text{-C}_3\text{N}_4$ and NaTaO_3 , the binary catalyst shows distinct intensive absorption in visible light region in contrast to the pure $g\text{-C}_3\text{N}_4$ and NaTaO_3 . The enhanced absorbing ability could be attributed to the formation of heterojunction between two pure semiconductors [26]. Moreover, with the introduction of Ag nanoparticles, the ternary catalyst exhibits a broad absorption in visible light region, even extending to 800 nm (NIR region), which can be assigned to the surface plasmon resonance (SPR) effect of the Ag nanoparticles on the surface of the catalyst. The $\text{Ag/g-C}_3\text{N}_4/\text{NaTaO}_3$ photocatalysts have a strong absorption under UV, visible and near-infrared light irradiation, which makes it possible to achieve the wide-spectrum utilization.

In addition, the band gap energies of semiconductors can be calculated by Kubelka–Munk equation [27]:

$$(ah\nu)^{1/n} = A(h\nu - E_g) \quad (1)$$

where α represents the absorption coefficient, h is the Planck constant, ν is the light frequency, A is a constant, E_g is the band gap energy and n depends on the optical transition type in semiconductor. The constant n equals 1/2 in direct gap semiconductor and 2 in indirect gap semiconductor, respectively. And the value of n for NaTaO_3 and $g\text{-C}_3\text{N}_4$ were both determined to be 1/2 due to their direct bandgaps. As shown in Fig. 3B, the bandgaps of the samples were estimated to be 3.87 eV and 2.74 eV corresponding to NaTaO_3 and $g\text{-C}_3\text{N}_4$, respectively, which were close to the known values in previous reports [28,29]. Furthermore, the XPS valence band spectra were also measured to evaluate the valence band (VB) edge position of NaTaO_3 and $g\text{-C}_3\text{N}_4$ (Fig. 3C). The VB potentials of NaTaO_3 and $g\text{-C}_3\text{N}_4$ were estimated to be 3.01 eV and 1.38 eV, respectively. The conduction band (CB) edge position could be calculated by the equations as follow [30]:

$$E_{CB} = E_{VB} - E_g \quad (2)$$

The CB potentials of NaTaO_3 and $g\text{-C}_3\text{N}_4$ were calculated to be -0.86 eV and -1.36 eV, respectively. In addition, the Mott-Schottky (MS) plot was measured under frequency of 750 Hz in the dark to estimate the flat band potential (U_{fb}) and the p-n type of NaTaO_3 and $g\text{-C}_3\text{N}_4$ [31]. Fig. 3D shows the MS plots of pure NaTaO_3 and $g\text{-C}_3\text{N}_4$. Apparently, both the linear MS plots of NaTaO_3 and $g\text{-C}_3\text{N}_4$ have a positive slope and indicate the n-type nature ($E_{CB} \approx U_{fb} - 0 \sim 0.2$ V).

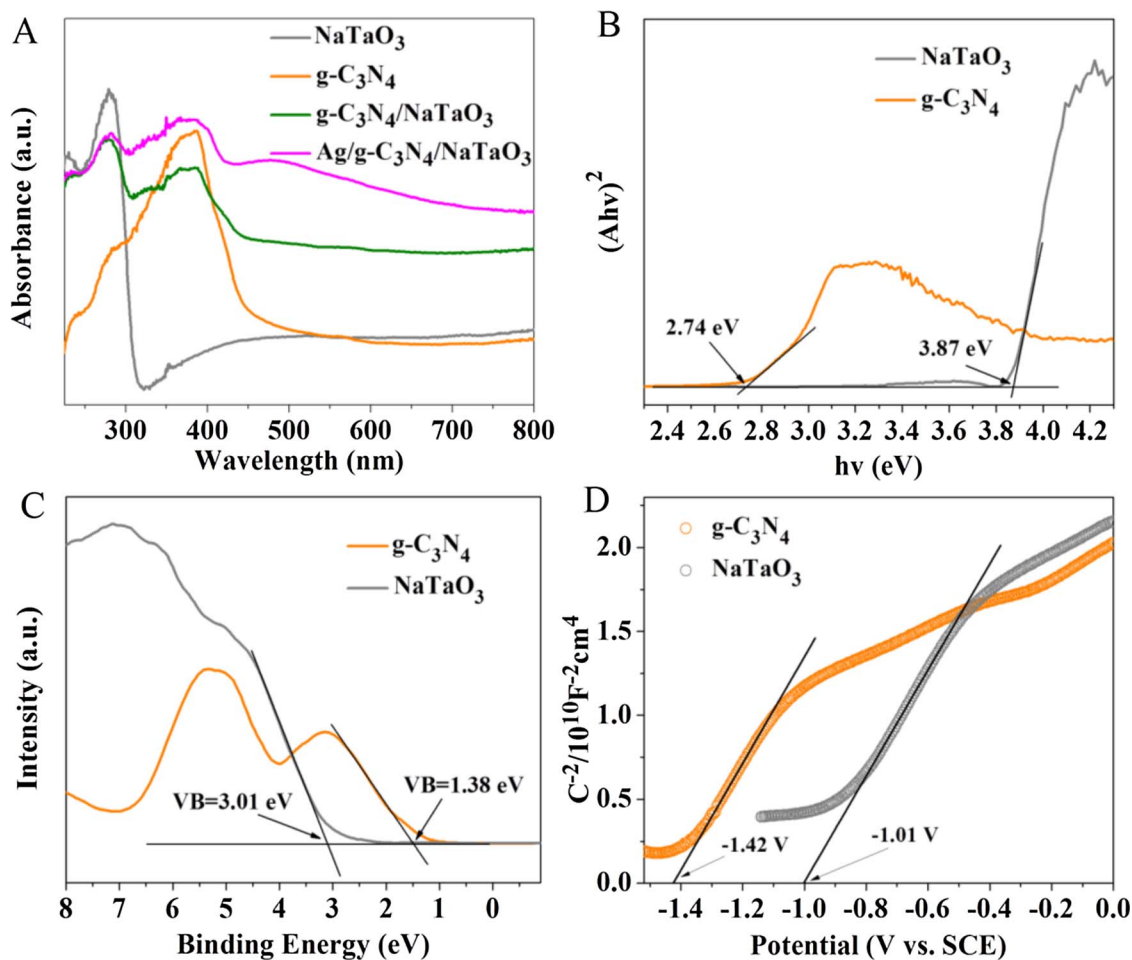


Fig. 3. UV-vis diffuse reflectance spectra of as-prepared samples (A); the transformed diffuse reflectance spectra (B), the XPS valence band spectra (C) and the Mott-Schottky plot (D) of NaTaO₃ and g-C₃N₄ samples.

The U_{fb} can be approximately determined as an x-intercept in the MS plot. The U_{fb} of the samples are -1.01 V and -1.42 V vs SCE which are equal to -0.77 V and -1.18 V vs NHE (Normal Hydrogen Electrode) for NaTaO₃ and g-C₃N₄. As the CB is generally considered to be $0-0.2$ V lower than U_{fb} , the calculation results were well consistent with the previous calculated CB value.

To uncover the correlation between composite materials and electron-hole separation efficiency of photocatalysts, room temperature PL spectroscopy were performed for the four samples [32]. As shown in Fig. 4A, pure NaTaO₃ did not show distinct photoluminescence property, and the corresponding signals of the single, binary and ternary samples could be listed as follows: Ag/g-C₃N₄/NaTaO₃ < g-C₃N₄/NaTaO₃ < g-C₃N₄. As the weaker fluorescence intensity represents higher carrier separation rates, the ternary Ag/g-C₃N₄/NaTaO₃ catalyst showed excellent carrier separation ability compared with the other catalysts, which means that the heterojunction between two pure catalysts and the introduction of Ag nanoparticles effectively impeded the recombination of photogenerated electrons and holes.

Electrochemical impedance spectroscopy (EIS) measurement was performed to study the electron transfer ability of the prepared catalysts, and the smaller radius of the EIS curve represents the lower resistance [33]. As evidenced by the EIS in Fig. 4B, the ternary Ag/g-C₃N₄/NaTaO₃ catalyst showed a marked reduction in electrochemical impedance compared to the pure g-C₃N₄, NaTaO₃ and binary g-C₃N₄/NaTaO₃ catalysts, which was favorable for the transport and separation of photogenerated electron-hole pairs.

Furthermore, the transient photocurrent responses of prepared samples were tested under visible light irradiation to study the

photocurrent response and electrons migration properties [34], and the current-time curves with 5 cycles of light irradiation on-off are displayed in Fig. 4C. Under visible light irradiation, pure NaTaO₃ almost could not show the electrical signal response due to its wide bandgap, which was consistent with the previous UV-vis DRS studies. It is clear that the g-C₃N₄/NaTaO₃ catalysts showed a significant enhanced photocurrent density than pure samples, and the Ag/g-C₃N₄/NaTaO₃ catalyst exhibited the strongest photocurrent response among all catalysts, which effectively clarified that the heterojunction between g-C₃N₄ and NaTaO₃ and the SPR of Ag nanoparticles on the surface of catalysts could contribute to enhancing the separation efficiency of the photo-generated electrons and holes, coinciding with the conclusion of the PL analysis. Based on the PL, EIS and photocurrent responses results, there is no doubt that the recombination of photogenerated electron-hole pairs can be significantly prevented by constituting heterojunctions and introducing Ag nanoparticles, which could certainly enhance the pollutant degradation efficiency. And the conclusion had been confirmed by the degradation experiment.

3.3. Adsorption capacity of obtained photocatalysts

As is well-known, larger specific surface area of catalyst could give it more active sites, and the adsorption of pollutants can help enhance the degradation speed. So the N₂ sorption analysis was performed to measure the specific surface area of prepared samples. From the nitrogen sorption isotherms displayed in Fig. S3, pure g-C₃N₄ has the highest specific surface area due to its ultrathin nanosheet structure. And the BET surface areas of pure NaTaO₃, g-C₃N₄/NaTaO₃ and Ag/g-

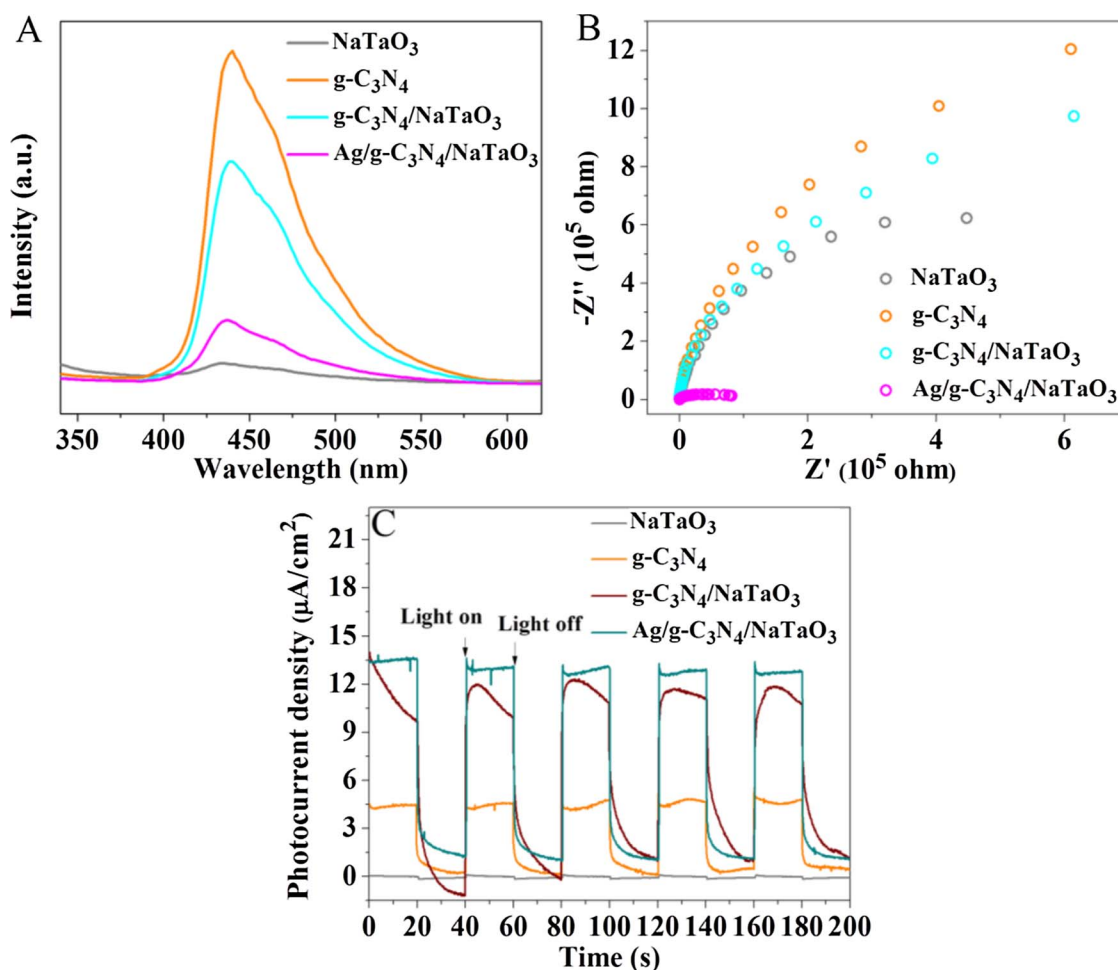


Fig. 4. Characterizations for the photoelectric property of as-prepared samples. (A) Room-temperature PL spectra, (B) electrochemical impedance spectra and (C) photocurrent response density of as-prepared samples.

$C_3N_4/NaTaO_3$ are calculated to be 137.475, 142.926 and 152.178 m^2/g , respectively, which indicates that the introduction of $g-C_3N_4$ nanosheets and Ag nanoparticles could effectively enhance the specific surface area of $NaTaO_3$. The enhancement of specific area can improve the adsorption capacity of catalysts and provide more active sites, and therefore the degradation speed was enhanced.

3.4. Photocatalytic performance

3.4.1. Optimal proportion of $g-C_3N_4$ and Ag

The $g-C_3N_4$ nanosheets and Ag nanoparticles were introduced to enhance the efficiency of light absorption and electron-hole separation. The as-prepared $NaTaO_3$, $g-C_3N_4$ and $g-C_3N_4/NaTaO_3$, $Ag/g-C_3N_4/NaTaO_3$ with different mass ratio were used to degrade TC under visible light irradiation. And the results of the degradation test are shown in Fig. S4. The ordinate C/C_0 represents the TC concentration ratio, and C_0 and C stand for the initial and remnant concentrations of the TC solutions. Fig. S4A shows the TC degradation after photocatalytic activity of $g-C_3N_4/NaTaO_3$ with different mass ratios of $g-C_3N_4$ nanosheets. From the degradation results, the pure $NaTaO_3$ almost could not degrade the TC under visible light irradiation, and the pure $g-C_3N_4$ degraded TC by about 56% after 1 h irradiation. The $g-C_3N_4/NaTaO_3$ photocatalysts showed excellent photocatalytic activity compared with pure $NaTaO_3$ and $g-C_3N_4$ under identical conditions. The 5 wt% $g-C_3N_4/NaTaO_3$ showed the best degradation rate of TC by about 80.76%, and the photocatalytic activity decreased with the further increased weight percent of $g-C_3N_4$. The $g-C_3N_4$ loaded on the surface of $NaTaO_3$ could promote the utilization of visible light and help separating the

photoproduction electron-hole pairs. However, superfluous $g-C_3N_4$ acted as a recombination center for electrons and holes, leading to lower photocatalytic activity.

Furthermore, metallic Ag nanoparticles were deposited on 5 wt% $g-C_3N_4/NaTaO_3$ photocatalysts to further improve the visible and near infrared light absorption via its surface plasmon resonance interaction. Fig. S4B displays the photocatalytic activity of $Ag/g-C_3N_4/NaTaO_3$ with different mass ratios of Ag nanoparticles for degradation of TC under visible light irradiation. The degradation results indicate that the photocatalytic activity further increased when the Ag nanoparticles were introduced, owing to the SPR and electronic bridge effect of the Ag nanoparticles. The photocatalysts showed the best degradation efficiency when the mass ratio of Ag was 0.5%. With the further increase of Ag, the degradation efficiency decreased slightly. This is because excess Ag will act as the recombination center, thus decreasing the photocatalytic performance.

3.4.2. Photocatalytic degradation of TC, RhB and phenol under different light conditions

The degradation experiment of TC was performed under UV light, visible light and near infrared light to test the wide-spectrum photocatalysis of as-prepared photocatalysts, and the degradation results are shown in Fig. 5. The experimental result (Fig. 5A–F) illustrates the photodegradation efficiencies of TC over pure $NaTaO_3$, $g-C_3N_4$, $g-C_3N_4/NaTaO_3$ and $Ag/g-C_3N_4/NaTaO_3$ catalysts under light irradiation with different wavelengths. The prepared photocatalysts showed excellent degradation activity under UV light irradiation (Fig. 5A). About 70.11% and 87.76% of TC was removed in 60 min over pure $NaTaO_3$ and pure

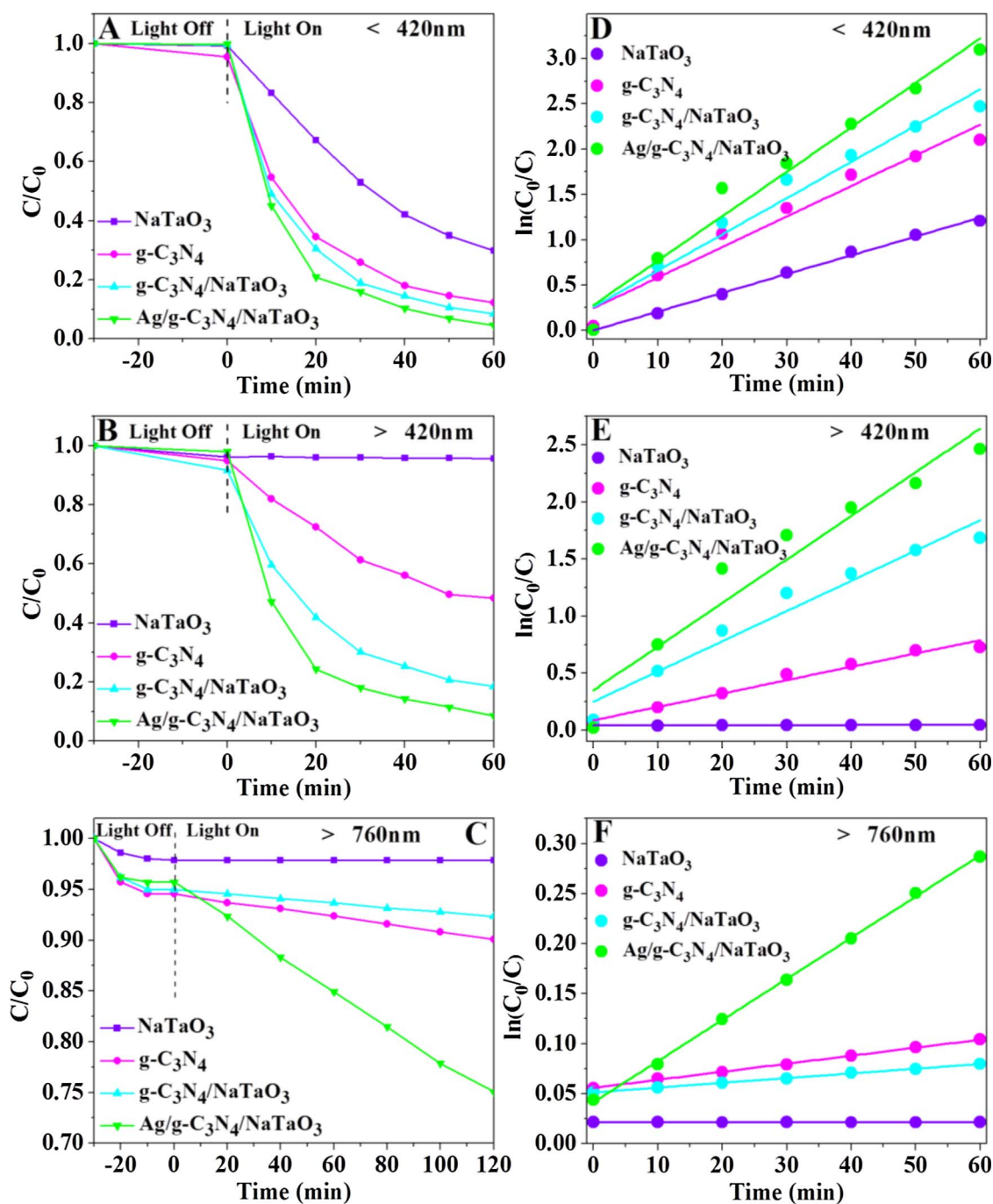


Fig. 5. Photocatalytic activities of as-prepared photocatalysts under (A) UV light, (B) visible light and (C) near-infrared light irradiation and corresponding reaction kinetic curves (D), (E) and (F).

g-C₃N₄, respectively, and the degradation rate increased to 91.54% after combining NaTaO₃ with g-C₃N₄, which might be attributed to the higher electron-hole separation rate caused by the heterojunction between NaTaO₃ and g-C₃N₄. The degradation rate was further improved to 95.47% after Ag nanoparticles were introduced. Trace amounts of Ag nanoparticles can enhance the light absorption of catalyst and promote the generation of electron-hole pairs. Fig. 5B shows the photo-degradation experiment of TC under visible light irradiation ($\lambda > 420$ nm). The degradation efficiency of prepared photocatalysts decreased to different extent, which could be ascribed to the low utilization rate of visible light over wide bandgap catalysts. The pure NaTaO₃ only slightly removed TC through adsorption under visible light. And the degradation efficiency of TC was 51.74% for pure g-C₃N₄

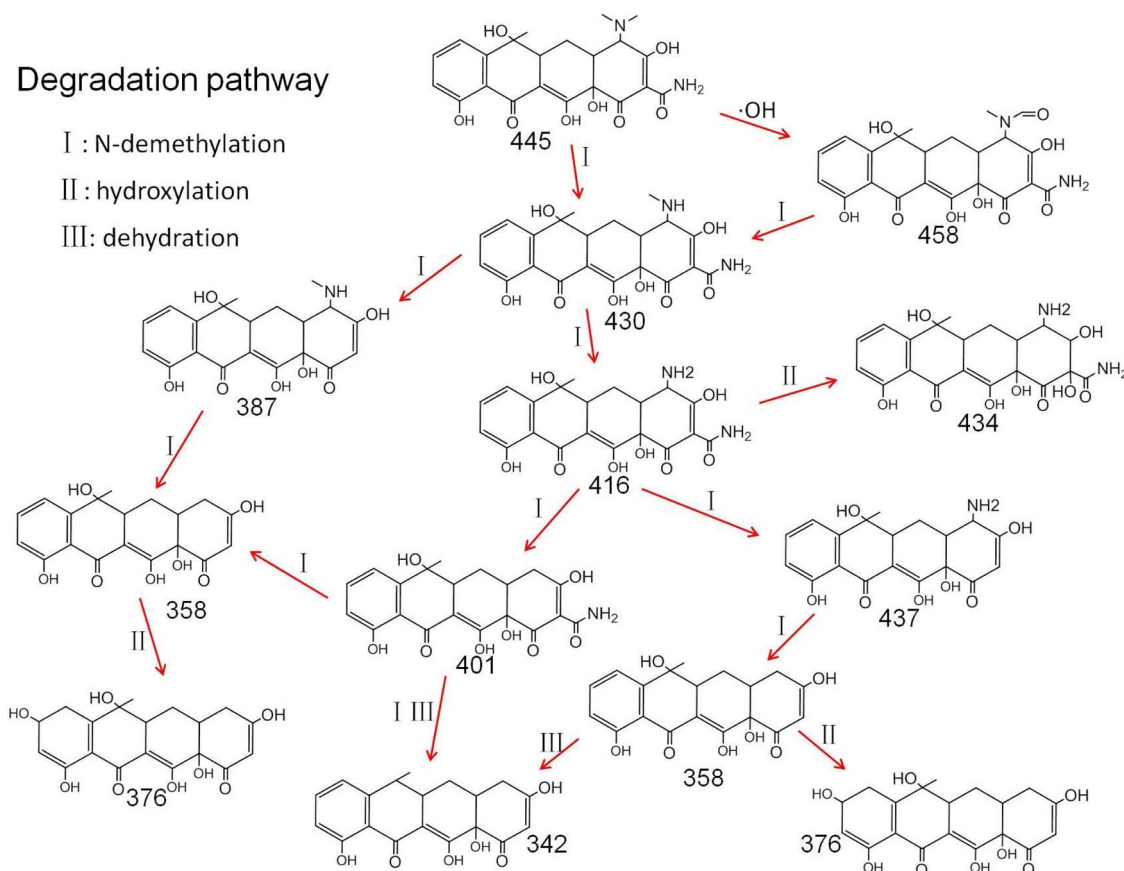
nanosheets. However, the photocatalytic performance of g-C₃N₄/NaTaO₃ and Ag/g-C₃N₄/NaTaO₃ just declined slightly compared with the results under UV light irradiation. The degradation rate of TC declined from 91.54% and 95.47% to 82.46% and 91.48% over g-C₃N₄/NaTaO₃ and Ag/g-C₃N₄/NaTaO₃ photocatalysts, respectively. The Ag/g-C₃N₄/NaTaO₃ still acted as the most efficient photocatalyst compared with the prepared pure and binary photocatalysts. The pure and binary catalysts could hardly remove TC under near infrared light irradiation ($\lambda > 760$ nm). Although the photocatalytic performance of ternary Ag/g-C₃N₄/NaTaO₃ catalyst also declined significantly, it was still observed that the concentration of TC decreased obviously (Fig. 5C), because the introduction of Ag nanoparticles could effectively increase the long wavelength light absorption performance of catalysts. The

experimental results indicated that the prepared Ag/g-C₃N₄/NaTaO₃ photocatalysts can be activated by wide-spectrum light and make the best use of natural light. Fig. 5D–F shows the reaction kinetic curves of TC degradation under different light condition for the samples of NaTaO₃, g-C₃N₄, g-C₃N₄/NaTaO₃ and Ag/g-C₃N₄/NaTaO₃, from which, the apparent kinetic constants for Ag/g-C₃N₄/NaTaO₃ can be found to be the highest of all samples under both UV, visible and near infrared light irradiation. This result could be attributed to the excellent reactivity of photogenerated carriers in the ternary Ag/g-C₃N₄/NaTaO₃ system, which demonstrates that this ternary photocatalyst can effectively protect the high reactivity of photogenerated carriers.

The main intermediate products were identified by LC–MS technique and the MS spectra of possible intermediates at different reaction time were displayed in Fig. S6. It can be seen that different *m/z* peaks appeared with the reaction progressed, which indicates that different intermediate products were generated during the reaction. The molecular weights and corresponding possible molecular structures are listed in Table S1. According to the quantity change of intermediates in the reaction process, the photodegradation of TC was supposed by three ways, the *N*-demethylation, hydroxylation and dehydration process, and the possible degradation pathway of TC can be roughly inferred (Scheme 1). Specifically, the low bond energy of N–C provide the possibility for the occurrence of *N*-demethylation, and a series of products with *m/z* of 430, 458, 416, 387, 401, 437 and 358 were generated by gradual fracture of C–N bonds. With the attack of ·OH, the hydroxylation and dehydration process occurred, which led to the generation of intermediates with *m/z* of 342, 376 and 434. Scheme 1 displayed the reasonable degradation pathway based on the above experimental dates, and these intermediates can be further decomposed into small molecular substances or even CO₂ and H₂O, which cannot be accurately determined. So this part of degradation will be concluded from the TOC removal test later.

Inorganic salts in water may have impacts on the degradation process [35–37], so some general inorganic ions were added to the supporting electrolyte to explore their influences on the photocatalytic degradation process. Fig. 6A and C display the degradation curves of TC in the presence of cations (Fe³⁺, Ca²⁺, Na⁺) and anions (Cl⁻, SO₄²⁻ and CO₃²⁻) under visible light irradiation. From Fig. 6A, it can be observed that the degradation rate is enhanced significantly with the presence of Fe³⁺. The apparent kinetic constants for Ag/g-C₃N₄/NaTaO₃ in the presence of Fe³⁺, Ca²⁺ and Na⁺ are 0.1043, 0.0231 and 0.0389 min⁻¹, respectively (Fig. 6B). Compared to the kinetic constants (0.0394 min⁻¹) without ion addition, the reaction rate was significantly enhanced in the presence of Fe³⁺. According to previous study, Fe³⁺ can enhance photocatalytic reactions by two ways. On one hand, Fe³⁺ can unite with photogenerated electrons and holes to form Fe²⁺ and Fe⁴⁺ ions and contribute to the electron-hole separation [38]. On the other hand, Fe³⁺ can act as an effective photosensitive substance and adsorb light to produce ·OH under weak acidic system, which resembles the photo-Fenton reactions and thus accelerates the degradation process [39,40]. The introduction of Na⁺ has little impact on the degradation, and the presence of Ca²⁺ inhibits the degradation process obviously by reacting with TC to form metal complexes [41]. From Fig. 6C, it can be seen that Cl⁻ and SO₄²⁻ show little impact in the degradation process, and the presence of CO₃²⁻ significantly suppresses the degradation process. The corresponding reaction kinetic curves are shown in Fig. 6D, and the apparent kinetic constant equals to 0.0116 min⁻¹ in the presence of CO₃²⁻, much lower than that without ion addition (0.0388 min⁻¹). This phenomenon was triggered by the scavenging effect of carbonate ions on hydroxyl radical according to the previous reports [42].

Furthermore, its degradation performances in RhB and phenol solutions were also investigated under different wavelength light irradiation. As shown in Fig. S5, Ag/g-C₃N₄/NaTaO₃ showed excellent



Scheme 1. Suggested photocatalytic degradation pathway of TC.

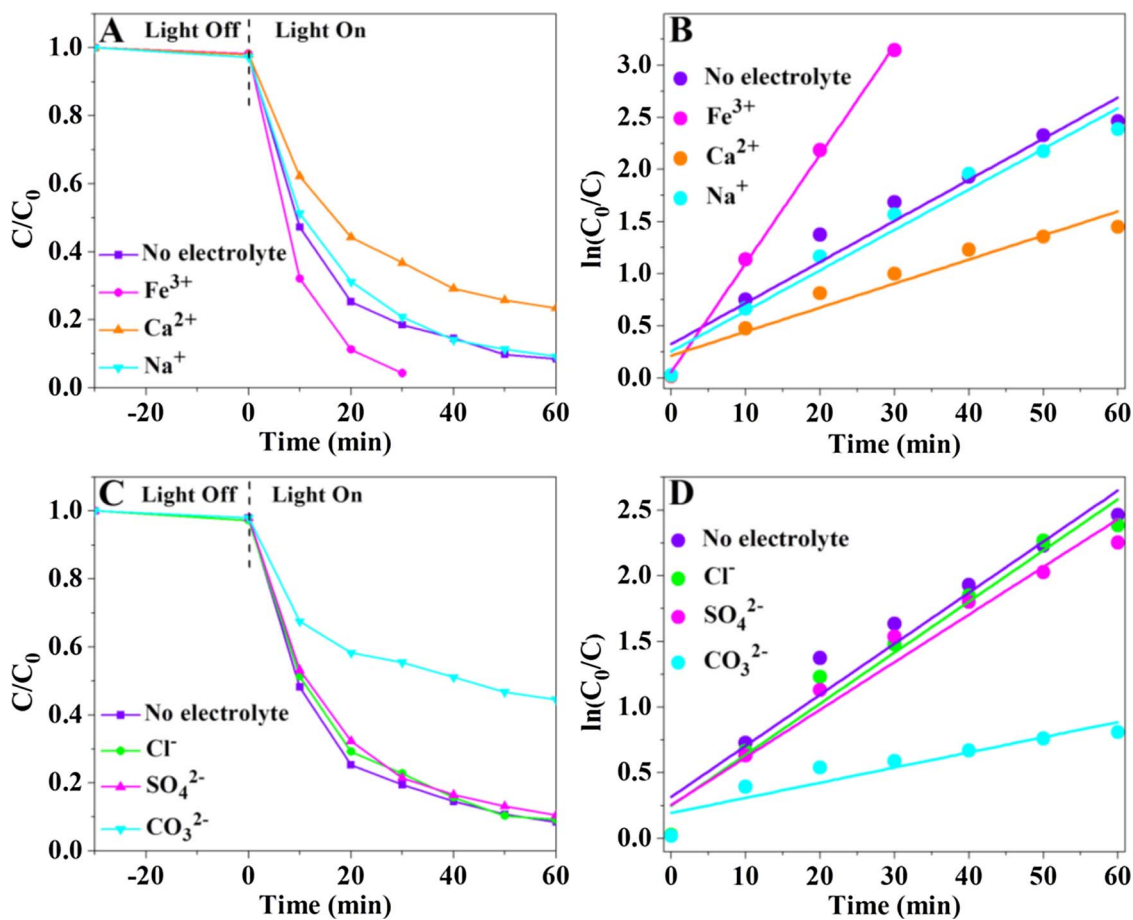


Fig. 6. Effects of coexisting ions on the degradation of TC over Ag/g-C₃N₄/NaTaO₃ photocatalyst under visible light irradiation and the corresponding reaction kinetic curves. (A, B) Cations: Fe³⁺, Ca²⁺ and Na⁺; (C, D) Anions: Cl⁻, SO₄²⁻ and CO₃²⁻.

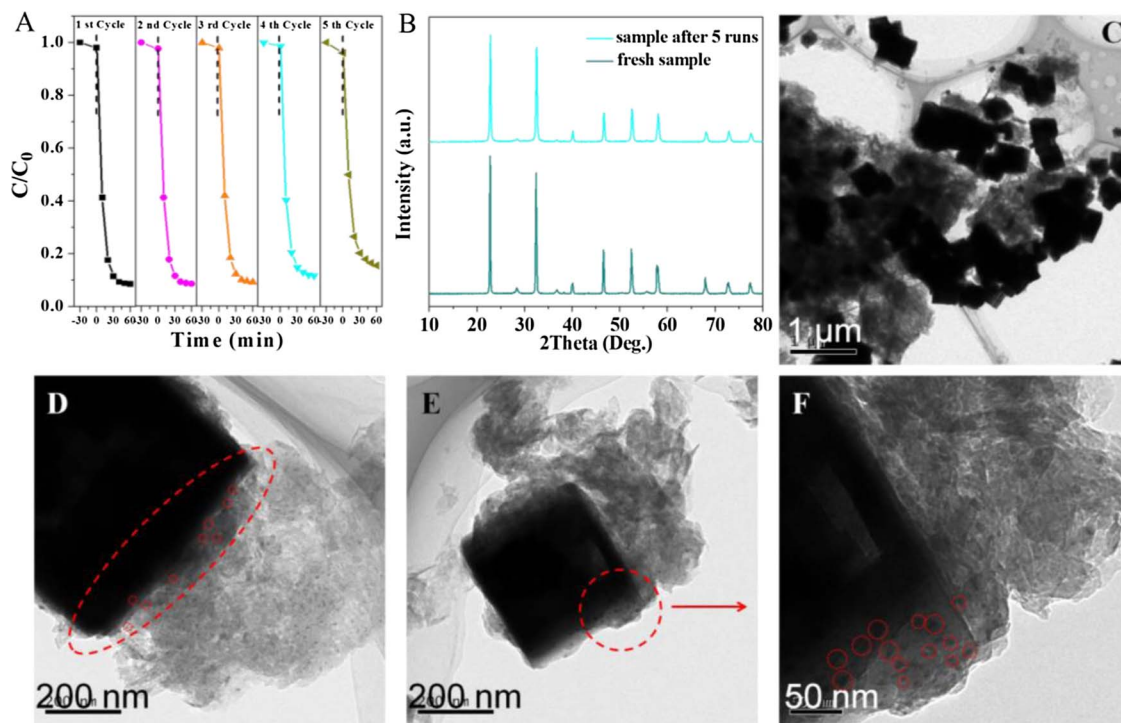


Fig. 7. Stability test of Ag/g-C₃N₄/NaTaO₃ photocatalyst. (A) Recycle experiments of Ag/g-C₃N₄/NaTaO₃ for the degradation of TC. (B) XRD patterns of Ag/g-C₃N₄/NaTaO₃ before and after 5 runs. (C-F) TEM images of Ag/g-C₃N₄/NaTaO₃ after 5 runs.

degradation effect towards RhB solution. The degradation rates under UV, visible and infrared light were 95.47%, 85.48% and 21.89%, respectively. In addition, phenol solution could also be degraded effectively over Ag/g-C₃N₄/NaTaO₃ catalyst, while the degrading rate of phenol solution was relatively decreased compared with RhB solution. The results satisfactorily indicated that the photocatalysts are widely applicable in degradation of many kinds of organic pollutants, such as antibiotics, dyes and many other persistent organic pollutants.

The comparisons of photocatalytic activities of Ag/g-C₃N₄/NaTaO₃ with other photocatalysts previously reported for the degradation of TC and RhB under visible light were listed in Table S2. Obviously, the Ag/g-C₃N₄/NaTaO₃ composite showed better degradation performance for TC than many reported materials, such as N-CNT/mpg-C₃N₄, PCNS/BiVO₄, CQDs/g-C₃N₄, h-BN/g-C₃N₄ and GQDs/mpg-C₃N₄. And furthermore, Ag/g-C₃N₄/NaTaO₃ also exhibited superior RhB degradation performance compared with a series of other NaTaO₃ or g-C₃N₄ based materials, such as Ag/AgCl/NaTaO₃, Ag₂O/NaTaO₃, S,N-GQDs/g-C₃N₄ and CQDs/g-C₃N₄. Based on the performance comparison with other materials, the superior performance for organic pollutants degradation of Ag/g-C₃N₄/NaTaO₃ can be further confirmed and displayed.

In order to study the mineralization ability of the photocatalysts, the total organic carbon (TOC) removal rate was also measured in this study. Fig. S5C shows the mineralization rate (TOC removal rate) of TC, RhB and phenol by the Ag/g-C₃N₄/NaTaO₃ photocatalyst under different light irradiation conditions, and the experimental results indicate that the prepared ternary photocatalyst showed great TOC removal capacity to all three TC, RhB and phenol under UV light or visible light irradiation. The excellent TOC removal efficiency illustrates the excellent mineralization ability of prepared ternary photocatalyst.

High stability is an important factor in the application of photocatalysts, in order to study the stability of the prepared ternary photocatalysts, the catalyst was recycled and repeatedly used 5 times. As shown in Fig. 7A, there is an obvious loss in the TC photodecomposition over Ag/g-C₃N₄/NaTaO₃ after 5 cycles. Moreover, XRD and XPS analysis were performed to characterize the samples before and after 5 cycle photocatalysis test. The XRD pattern of the recycled Ag/g-C₃N₄/NaTaO₃ have no obvious distinction compared with the original one (Fig. 7B), which suggests that the crystalline phase has not changed before and after reaction. The unaltered XPS spectra (Fig. S7) further indicate that the element composition and chemical state of Ag/g-C₃N₄/NaTaO₃ have not changed before and after reaction. The morphology of used Ag/g-C₃N₄/NaTaO₃ was further checked by TEM analysis (Fig. 7C–F). It can be seen that there was a slight agglomeration of the materials after five cycles of using, which may be the cause of the decrease in catalytic performance. But the morphology of the used catalyst has not changed. Especially, the Ag nanoparticles distributed on the contact surface of NaTaO₃ and g-C₃N₄ have not fallen off, indicating the high stability of prepared Ag/g-C₃N₄/NaTaO₃ photocatalysts.

3.5. Possible photocatalytic mechanism in reaction system

To reveal the photocatalytic mechanism of Ag/g-C₃N₄/NaTaO₃ in TC degradation process, several scavengers were used during the photocatalytic reaction. In this study, ethylenediaminetetraacetic acid disodium (EDTA-2Na) was used as scavenger of holes (h⁺), and isopropanol (IPA) and 1,4-benzoquinone (BQ) were added as scavengers for hydroxyl radical (·OH) and superoxide radical (·O₂⁻), respectively [43]. Fig. 8A and B represent the TC degradation curves in the presence of the above scavengers over g-C₃N₄/NaTaO₃ and Ag/g-C₃N₄/NaTaO₃. It is obvious that both g-C₃N₄/NaTaO₃ and Ag/g-C₃N₄/NaTaO₃ show great photocatalytic effect under visible light irradiation. The addition of IPA just caused a little inhibitory effect for g-C₃N₄/NaTaO₃, while the presence of BQ or EDTA-2Na shows obvious inactivation effect on g-C₃N₄/NaTaO₃ catalyst, which demonstrates that holes and ·O₂⁻ played important roles in the reaction process, and few ·OH was generated in

the TC photodegradation over g-C₃N₄/NaTaO₃. From Fig. 8B, all the three scavengers show significant deactivation effects on the ternary Ag/g-C₃N₄/NaTaO₃ photocatalyst, indicating that ·OH, ·O₂⁻ and holes all played important roles in the Ag/g-C₃N₄/NaTaO₃ photocatalytic reaction system. Based on these results, preliminary conclusions could be proposed that the introduction of Ag nanoparticles can help enhancing the generation of ·OH and improving the photocatalysis efficiency.

To further validate the radical generation in the photocatalytic system over g-C₃N₄/NaTaO₃ and Ag/g-C₃N₄/NaTaO₃, the ESR spin-trap technology [44–46] was also performed (Fig. 8C and D). Under UV light irradiation, the characteristic signals of DMPO·O₂⁻ and DMPO·OH can be observed, indicating the generation of ·O₂⁻ and ·OH during the photodegradation process. In addition, the characteristic signals of ·O₂⁻ and ·OH are also observed during reaction process over Ag/g-C₃N₄/NaTaO₃, and the signal intensities of both ·O₂⁻ and ·OH over Ag/g-C₃N₄/NaTaO₃ were much stronger than that over g-C₃N₄/NaTaO₃. The ternary Ag/g-C₃N₄/NaTaO₃ provides about double of the ·O₂⁻ signal strength and quadruple of the ·OH signal strength compared to the binary g-C₃N₄/NaTaO₃. Under visible light irradiation, a strong characteristic signal of DMPO·O₂⁻ can still be observed, while the signal of DMPO·OH is very weak. And it can also be observed that both the DMPO·O₂⁻ signal and DMPO·OH signal get enhanced after the introduction of Ag nanoparticles. The results indicated that the introduction of Ag nanoparticles could indeed enhance the generation of ·O₂⁻ and ·OH under both UV and visible light irradiation, which can also explain the hugely enhanced photocatalytic performance after introducing Ag nanoparticles.

Based on the above experimental results, a logical explanation for the photocatalytic mechanism of binary g-C₃N₄/NaTaO₃ heterogeneous and Ag/g-C₃N₄/NaTaO₃ photocatalysts could be proposed. The mechanism will be discussed in UV and visible light separately.

According to the ESR measure, the characteristic signals of both ·O₂⁻ and ·OH are very strong for Ag/g-C₃N₄/NaTaO₃ under UV light irradiation, suggesting that a large amount of electrons and holes may actively participate the radical generation reaction in the CB of g-C₃N₄ and VB of NaTaO₃. Hence, we have reason to believe that the electron transfer follows the Z-scheme mechanism in Ag/g-C₃N₄/NaTaO₃. However, for g-C₃N₄/NaTaO₃, the ESR single of ·OH sharp dropped under UV light irradiation (less than a quarter of Ag/g-C₃N₄/NaTaO₃), while the single of ·O₂⁻ was still sufficiently strong (about half of Ag/g-C₃N₄/NaTaO₃). The decrease of radical generation reflects the decreased activity of electrons and holes, and thus it is reasonable to presume that a large amount of electrons (holes) shifted from the high-energy CB of g-C₃N₄ (VB of NaTaO₃) to the low-energy CB of NaTaO₃ (VB of g-C₃N₄). Thus it can be concluded that an ordinary double-transfer mechanism is more suitable for explaining the charge transfer process in g-C₃N₄/NaTaO₃.

The mechanism under UV light irradiation is shown in Scheme 2A. For g-C₃N₄/NaTaO₃, the transfer process of photogenerated carriers could be classified to a typical double-transfer mechanism in heterojunction structure. The photogenerated electrons from the CB of g-C₃N₄ could transfer to the CB of NaTaO₃. Meanwhile, the photogenerated holes from the VB of NaTaO₃ could transfer to the VB of g-C₃N₄. Hence, the photogenerated electrons and holes could be collected on the CB of NaTaO₃ and VB of g-C₃N₄, respectively, which significantly enhanced the separation of photogenerated carriers and photocatalytic activity. However, the potential of OH⁻/·OH couples is about +2.4 eV and much higher than the VB of g-C₃N₄ [47,48], so when the photogenerated holes transferred from the VB of NaTaO₃ to the VB of g-C₃N₄, they lost the ability to oxidize H₂O into ·OH. The characteristic signals of DMPO·OH of g-C₃N₄/NaTaO₃ under UV light belong to the ·OH generated in another way: the ·O₂⁻ generated on the CB of NaTaO₃ can react with H⁺ to form ·OH. Thus the ordinary double-transfer mechanism in binary g-C₃N₄/NaTaO₃ heterojunction cannot protect the high potential CB of NaTaO₃ and make the best use of it. On the other

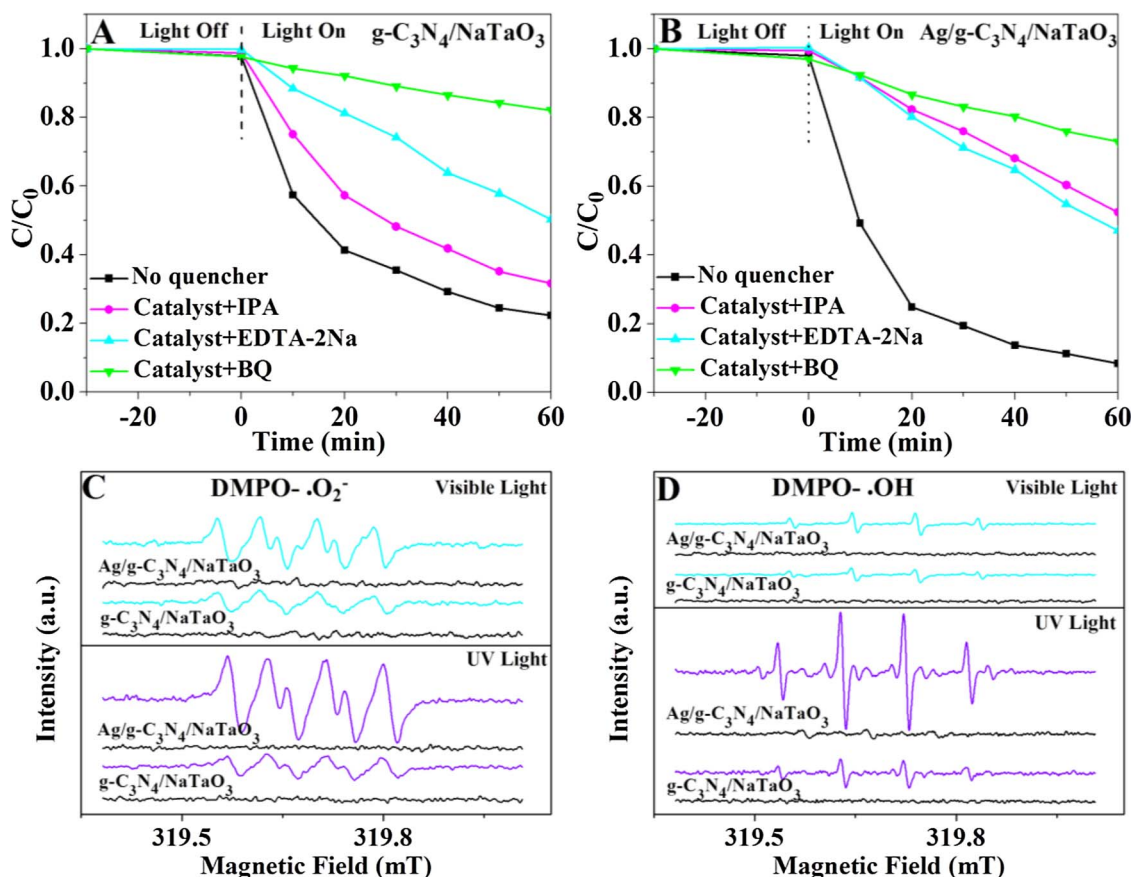
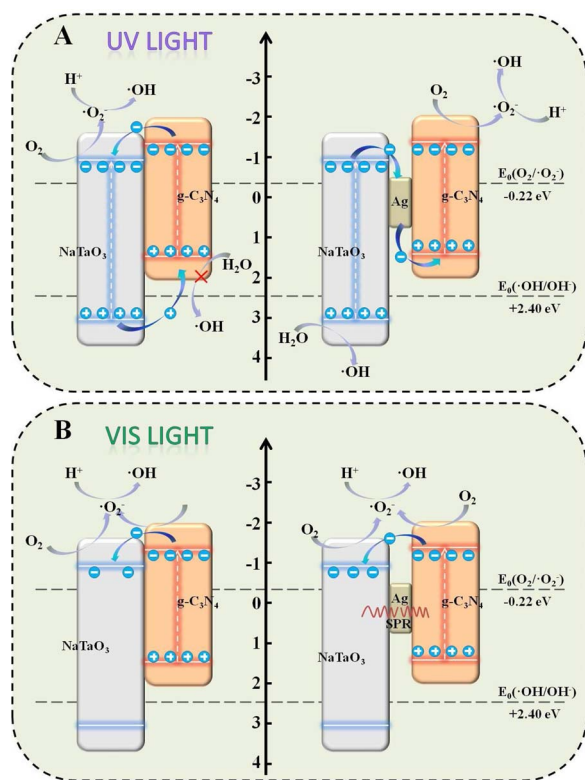


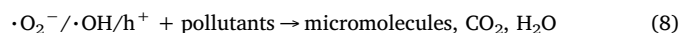
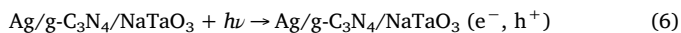
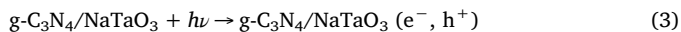
Fig. 8. Degradation curves of TC with additions of scavengers under visible light over (A) $g\text{-C}_3\text{N}_4/\text{NaTaO}_3$ and (B) $\text{Ag}/g\text{-C}_3\text{N}_4/\text{NaTaO}_3$. DMPO spin-trapping ESR spectra for (C) $\text{DMPO}\cdot\text{O}_2^-$ and (D) $\text{DMPO}\cdot\text{OH}$ under different light condition.



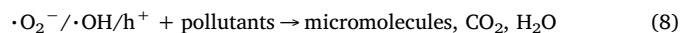
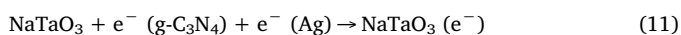
Scheme 2. Schematic diagram for the charge separation under (A) UV light and (B) visible light irradiation.

hand, it is clear to know from previous studies that the photogenerated carrier separation rate of ternary $\text{Ag}/g\text{-C}_3\text{N}_4/\text{NaTaO}_3$ is much higher than that of binary $g\text{-C}_3\text{N}_4/\text{NaTaO}_3$, and the generation of both $\cdot\text{O}_2^-$ and $\cdot\text{OH}$ in $\text{Ag}/g\text{-C}_3\text{N}_4/\text{NaTaO}_3$ reaction system get tremendously enhanced compared to $g\text{-C}_3\text{N}_4/\text{NaTaO}_3$. Hence, for $\text{Ag}/g\text{-C}_3\text{N}_4/\text{NaTaO}_3$, the Z-scheme transfer mechanism is a much more plausible explanation for the transfer process of photogenerated carriers. As shown in Scheme 2A, the photogenerated electrons on the VB of NaTaO_3 and holes on the CB of $g\text{-C}_3\text{N}_4$ would transfer to metallic Ag nanoparticles due to its Schottky barriers at the metal-semiconductor interfaces. These electrons and holes recombined in the Ag nanoparticles, and the remaining electrons and holes accumulated at the CB of $g\text{-C}_3\text{N}_4$ and VB of NaTaO_3 , respectively, which successfully protected the highly positive VB of NaTaO_3 and negative CB of $g\text{-C}_3\text{N}_4$ and greatly enhanced the electron-hole separation rate and photocatalytic activity. In addition, the Ag nanoparticles could absorb light and produce photo-induced electrons due to its SPR effect, and these photo-induced electrons could shift to NaTaO_3 and $g\text{-C}_3\text{N}_4$ and enhance the photocatalytic activity. In this way, the photogenerated holes on the VB of NaTaO_3 have enough energy to oxidize H_2O or OH^- into $\cdot\text{OH}$, and the accumulated electrons on the CB of $g\text{-C}_3\text{N}_4$ have stronger reducibility and can generate more $\cdot\text{O}_2^-$, which can be demonstrated by the ESR test (Fig. 8C and D). The all generated h^+ , $\cdot\text{O}_2^-$ and $\cdot\text{OH}$ could react with organic pollutant and degrade them into smaller intermediate products or even into end products like H_2O and CO_2 . In brief, the introduction of Ag nanoparticles can change the transfer process of photogenerated carriers to form a Z-scheme transfer mechanism, which can significantly enhance the electron-hole separation rate and effectively protect the high potential VB of NaTaO_3 and CB of $g\text{-C}_3\text{N}_4$. Meanwhile, another possible charge transfer pathway for $\text{Ag}/g\text{-C}_3\text{N}_4/\text{NaTaO}_3$ based on the electron capture effect of Ag nanoparticles was discussed in the Supporting

information (Scheme S1).



As NaTaO₃ cannot be excited by visible light, the mechanism under visible light irradiation can be illustrated in Scheme 2B. In g-C₃N₄/NaTaO₃ system, the g-C₃N₄ absorbs the visible light to produce electron-hole pairs. A part of photogenerated electrons on the CB of g-C₃N₄ transfer to the dissolved oxygen to form $\cdot\text{O}_2^-$ because the CB of g-C₃N₄ is lower than the E₀ (O₂/O₂⁻). And a part of photogenerated electrons will transfer to the CB of NaTaO₃, which can enhance the separation of electrons and holes, and the electrons on the surface of NaTaO₃ still have the ability to reduce molecular oxygen into $\cdot\text{O}_2^-$ (proved by the ESR analysis shown in Fig. S8). The $\cdot\text{O}_2^-$ free radical can directly degrade TC molecules or form $\cdot\text{OH}$ free radical to degrade TC. In Ag/g-C₃N₄/NaTaO₃ system, not only can g-C₃N₄ produce electron-hole pairs, but also the Ag nanoparticles can absorb the visible light to produce electron-hole pairs by SPR. The photogenerated electrons on Ag nanoparticles could transfer to the CB of g-C₃N₄ and NaTaO₃, which makes the photogenerated electron density on Ag/g-C₃N₄/NaTaO₃ much higher than g-C₃N₄/NaTaO₃. Besides, the photogenerated electrons on g-C₃N₄ can also transfer to the CB of NaTaO₃ to inhibit the recombination of charges. In the summary, the combination of NaTaO₃ and g-C₃N₄ enhances the charge separation and the introduction of Ag nanoparticles significantly improves the visible light utilization.



4. Conclusions

In this study, a ternary Ag/g-C₃N₄/NaTaO₃ photocatalyst was successfully synthesized through hydrothermal, sintering, wet-impregnation and photodeposition methods. The prepared samples were characterized by XRD, SEM, TEM, FTIR and XPS measurements. The photocatalytic activity was tested by degrading TC, RhB, and phenol under UV light, visible light and near infrared light irradiation. The Ag/g-C₃N₄/NaTaO₃ composites showed enhanced photocatalytic activity under wide-spectrum light irradiation than pure and binary particles. The Ag nanoparticles on the surface of catalysts acted as a charge excitation and transfer center, and changed the transfer process of photogenerated carriers to form a Z-scheme transfer mechanism. The enhanced photocatalytic performance can be attributed to the great charge excitation ability, efficient charge separation rate and the utilization of high potential VB of NaTaO₃ and CB of g-C₃N₄. In addition, the photocatalyst exhibited great stability with little loss of activity after five runs reaction. Fe³⁺ showed a positive role in degradation process, and the presence of Ca²⁺ and CO₃²⁻ could partly obstruct the

degradation process. In general, the ternary Ag/g-C₃N₄/NaTaO₃ photocatalyst has strong wide-spectrum light absorbance and exhibits efficient photocatalytic activity to organic pollutants. This study could provide a direction for constructing novel efficient photocatalysts.

Acknowledgments

The study was financially supported by Projects 51579096, 51521006, 51222805, 51409024 and 51709103 supported by National Natural Science Foundation of China, the Key Research and Development Program of Hunan Province of China (2017SK2241), and the National Program for Support of Top-Notch Young Professionals of China (2012).

Appendix A. Supplementary data

Supplementary material related to this article can be found, in the online version, at doi:<https://doi.org/10.1016/j.apcatb.2018.02.031>.

References

- [1] Y. Deng, L. Tang, G. Zeng, J. Wang, Y. Zhou, J. Wang, J. Tang, L. Wang, C. Feng, J. Colloid Interface Sci. 509 (2017) 219–234.
- [2] J. Wang, L. Tang, G. Zeng, Y. Liu, Y. Zhou, Y. Deng, J. Wang, B. Peng, ACS Sustain. Chem. Eng. 5 (2017) 1062–1072.
- [3] W. Zheng, K. Teramura, S. Hosokawa, T. Tanaka, Appl. Catal. B: Environ. 163 (2015) 241–247.
- [4] H. Lin, L. Li, M. Zhao, X. Huang, X. Chen, G. Li, R. Yu, J. Am. Chem. Soc. 134 (2012) 8328.
- [5] J. Wang, P. Wang, Y. Cao, J. Chen, W. Li, Y. Shao, Y. Zheng, D. Li, Appl. Catal. B: Environ. 136–137 (2013) 94–102.
- [6] X. Qian, D. Yue, Z. Tian, R. Meng, Y. Zhu, M. Kan, T. Zhang, Y. Zhao, Appl. Catal. B: Environ. 193 (2016) 16–21.
- [7] H. Li, Y. Liu, Y. Cui, W. Zhang, C. Fu, X. Wang, Appl. Catal. B: Environ. 183 (2016) 426–432.
- [8] S. Kumar, A. Baruah, S. Tonda, B. Kumar, V. Shanker, B. Sreedhar, Nanoscale 6 (2014) 4830.
- [9] D. Xu, W. Shi, C. Song, M. Chen, S. Yang, W. Fan, B. Chen, Appl. Catal. B: Environ. 191 (2016) 228–234.
- [10] J. Ke, J. Liu, H. Sun, H. Zhang, X. Duan, P. Liang, X. Li, M.O. Tade, S. Liu, S. Wang, Appl. Catal. B: Environ. 200 (2017) 47–55.
- [11] M. Humayun, Q. Yang, F. Raziq, Y. Rui, Z. Li, X. Zhang, L. Jing, Environ. Sci. Technol. 22 (2016) 13600–13610.
- [12] T. Liu, B. Liu, L. Yang, X. Ma, H. Li, S. Yin, T. Sato, T. Sekino, Y. Wang, Appl. Catal. B: Environ. 204 (2017) 593–601.
- [13] H. Tada, T. Mitsui, T. Kiyonaga, T. Akita, K. Tanaka, Nat. Mater. 5 (2006) 782.
- [14] Y. Deng, L. Tang, G. Zeng, C. Feng, H. Dong, J. Wang, H. Feng, Y. Liu, Y. Zhou, Y. Pang, Environ. Sci.: Nano 4 (2017).
- [15] Y. Deng, L. Tang, G. Zeng, Z. Zhu, M. Yan, Y. Zhou, J. Wang, Y. Liu, J. Wang, Appl. Catal. B: Environ. 203 (2017) 343–354.
- [16] Y. Deng, L. Tang, G. Zeng, H. Dong, M. Yan, J. Wang, W. Hu, J. Wang, Y. Zhou, J. Tang, Appl. Surf. Sci. 387 (2016) 882–893.
- [17] S. Yang, D. Xu, B. Chen, B. Luo, X. Yan, L. Xiao, W. Shi, Appl. Surf. Sci. 383 (2016) 214–221.
- [18] D. Xu, M. Chen, S. Song, D. Jiang, W. Fan, W. Shi, CrystEngComm 16 (2013) 1384–1388.
- [19] P. Niu, L. Zhang, G. Liu, H.M. Cheng, Adv. Funct. Mater. 22 (2012) 4763–4770.
- [20] B. Lin, G. Yang, B. Yang, Y. Zhao, Appl. Catal. B: Environ. 198 (2016) 276–285.
- [21] G. Zhang, G. Li, Z.A. Lan, L. Lin, A. Savateev, T. Heil, S. Zafeiratos, X. Wang, M. Antonietti, Angew. Chem. Int. Ed. 56 (2017) 1–6.
- [22] S. Yang, Y. Gong, J. Zhang, L. Zhan, L. Ma, Z. Fang, R. Vajtai, X. Wang, P.M. Ajayan, Adv. Mater. 25 (2013) 2452–2456.
- [23] X. She, H. Xu, Y. Xu, J. Yan, J. Xia, L. Xu, Y. Song, Y. Jiang, Q. Zhang, H. Li, J. Mater. Chem. A 2 (2014) 2563–2570.
- [24] Z. Zhang, D. Jiang, D. Li, M. He, M. Chen, Appl. Catal. B: Environ. 183 (2016) 113–123.
- [25] Y. Chen, W. Huang, D. He, Y. Situ, H. Huang, ACS Appl. Mater. Interface 6 (2014) 14405–14414.
- [26] C. Liu, T. Sun, L. Wu, J. Liang, Q. Huang, J. Chen, W. Hou, Appl. Catal. B: Environ. 170 (2015) 17–24.
- [27] X. Xin, J. Lang, T. Wang, Y. Su, Y. Zhao, X. Wang, Appl. Catal. B: Environ. 181 (2016) 197–209.
- [28] X. Wu, S. Yin, B. Liu, M. Kobayashi, M. Kakihana, T. Sato, J. Mater. Chem. A 2 (2014) 20832–20840.
- [29] J. Luo, G. Dong, Y. Zhu, Z. Yang, C. Wang, Appl. Catal. B: Environ. 214 (2017) 46–56.
- [30] F. Chen, Q. Yang, C. Niu, X. Li, C. Zhang, J. Zhao, Q. Xu, Y. Zhong, Y. Deng, G. Zeng, Catal. Commun. 73 (2016) 1–6.
- [31] B. Xu, P. He, H. Liu, P. Wang, G. Zhou, X. Wang, Angew. Chem. Int. Ed. 53 (2014)

- 2339–2343.
- [32] X. Wang, Y. Liang, W. An, J. Hu, Y. Zhu, W. Cui, *Appl. Catal. B: Environ.* 219 (2017) 53–62.
- [33] X. Jiao, Z. Chen, X. Li, Y. Sun, S. Gao, W. Yan, C. Wang, Q. Zhang, Y. Lin, Y. Luo, *J. Am. Chem. Soc.* 139 (2017) 7586.
- [34] Y. Ao, K. Wang, P. Wang, C. Wang, J. Hou, *Appl. Catal. B: Environ.* 194 (2016) 157–168.
- [35] S. Matsuo, N. Sakaguchi, K. Yamada, T. Matsuo, H. Wakita, *Appl. Surf. Sci.* 228 (2004) 233–244.
- [36] L. Tang, J. Wang, G. Zeng, Y. Liu, Y. Deng, Y. Zhou, J. Tang, J. Wang, Z. Guo, *Hazard. Mater.* 306 (2016).
- [37] J. Wiszniowski, D. Robert, J. Surmacz-Gorska, K. Miksch, S. Malato, J.V. Weber, *Appl. Catal. B: Environ.* 53 (2004) 127–137.
- [38] Y. Wu, J. Zhang, L. Xiao, F. Chen, *Appl. Catal. B: Environ.* 88 (2009) 525–532.
- [39] Y. Liu, W. Jin, Y. Zhao, G. Zhang, W. Zhang, *Appl. Catal. B: Environ.* 206 (2017) 642–652.
- [40] M. Yoon, Y. Oh, S. Hong, J.S. Lee, R. Boppella, H.K. Sun, F.M. Mota, O.K. Sang, H.K. Dong, *Appl. Catal. B: Environ.* 206 (2017) 263–270.
- [41] L. Jin, X. Amaya-Mazo, M.E. Apel, S.S. Sankisa, E. Johnson, M.A. Zbyszynska, A. Han, *Biophys. Chem.* 128 (2007) 185–196.
- [42] H. Xiao, R. Liu, X. Zhao, J. Qu, *J. Mol. Catal. A: Chem.* 286 (2008) 149–155.
- [43] J. Wang, L. Tang, G. Zeng, Y. Deng, Y. Liu, L. Wang, Y. Zhou, Z. Guo, J. Wang, C. Zhang, *Appl. Catal. B: Environ.* 209 (2017) 285–294.
- [44] H. Zhao, Y. Chen, Q. Peng, Q. Wang, G. Zhao, *Appl. Catal. B: Environ.* 203 (2017) 127–137.
- [45] S. Huang, Y. Xu, Q. Liu, T. Zhou, Y. Zhao, L. Jing, H. Xu, H. Li, *Appl. Catal. B: Environ.* 218 (2017) 174–185.
- [46] H. Zhao, L. Qian, Y. Chen, Q. Wang, G. Zhao, *Chem. Eng. J.* 332 (2018) 486–498.
- [47] S. Meng, X. Ning, T. Zhang, S.F. Chen, X. Fu, *Phys. Chem. Chem. Phys.* 17 (2015) 11577.
- [48] Y. Deng, L. Tang, G. Zeng, J. Wang, Y. Zhou, J. Wang, J. Tang, Y. Liu, B. Peng, F. Chen, *J. Mol. Catal. A: Chem.* 421 (2016) 209–221.